Impurity-Induced Robust Trionic Effect in Layered Violet Phosphorus

Yanyong Li[1], Songhua Cai[1], Wai Kin Lai[1], Chenhao Wang[1], Lukas Rogée[1], Lyuchao Zhuang[1], Lingling Zhai[1], Shenghuang Lin[1], Mingjie Li[1] and Shu Ping Lau[1,]*

Dr. Y. Y. Li, Dr. S. H. Cai, W. K. Lai, C. H. Wang, Dr. L. Rogée, L. C. Zhuang, Dr. L. L. Zhai, Dr. S. H. Lin, Dr. M. J. Li, Prof. S. P. Lau

[1].Department of Applied Physics, the Hong Kong Polytechnic University, Hung Hom, Kowloon, Hong Kong, P. R. China

E-mail: apsplau@polyu.edu.hk

Keywords: phosphorus allotrope, violet phosphorus, 2D layered material, photoluminescence, trion, stannous Sn-I-P impurities

Abstract

Trionic effect is a vital excitonic physical phenomenon, which intensively affects the optical and optoelectronic properties of two-dimensional materials. Violet phosphorus (VP) is another allotrope of elemental phosphorus with robust photoluminescence (PL) emission in the visible range. So far, the experimental investigation of the excitonic behavior in VP are quite scarce. Herein, we have investigated the evolution of the PL mechanism in synthesized VP crystals against the Ar^+ plasma exposure with emphasis on a conversion from trion to exciton emission. The estimated trion binding energy of VP is around 109 meV, relatively larger than common layered materials. By analyzing the chemical states and the atomic structures, the conversion mechanism is proposed as follows. The Ar^+ plasma treatment reduces the stannous Sn-I-P impurities' population, which are incorporated into the VP lattices and serve as the n-type dopants leading to the trion formation. Besides, various surface defects (PO_x) can promote the trion-to-exciton conversion by withdrawing electrons from VP in the process and act as hole-trap centers to enhance the photodetection of VP phototransistors. This work reveals that the layered VP crystal can provide an ideal platform to study the excitonic physics and future trionic devices at the 2D limit.

1. Introduction

Excitonic behavior plays an important role in the photoluminescence (PL) emission in two-dimensional (2D) materials. Because of the reduced dielectric screening, dimensional confinement and considerable carriers' effective mass in 2D materials, photo-excited free electron-hole pairs attract each other tightly through Coulomb interaction to form a bound quasi-particle named neutral exciton (X^0). As the exciton binding energy is strong enough in 2D materials (normally 10 ~ 200 meV), the PL properties of 2D materials are dominated mainly by diverse excitonic bound states.[1-4] Correspondingly, the exciton wave function is well localized in momentum space resulting in the remarkable optical and optoelectronic properties in 2D materials, such as the strong room-temperature PL and abundant valley-selective excitation of excitonic states in transition metal dichalcogenides (TMDs). [2, 4-7] Besides, a neutral exciton can capture an additional electron or hole to form a correlated three-particle state (e-e-h or h-e-h), known as a trion (T), in the presence of excess carriers.[8] It has been demonstrated that trionic effect can strongly affect the PL properties of 2D materials through controlling the excess carriers' population.[9-11] However, the small trion binding energy in various TMDs (< 50 meV) greatly hinders the investigation of T emission in 2D systems. Taking the thermal fluctuation and dimensional confinement into account, it is arduous for people to observe T emission in non-monolayer TMDs at room temperature.[12] Recently, the radiative recombination of X^0 and T in black phosphorus (BP) has been studied yet.[13] Robust T emission in monolayer BP was observed at ~ 1.63 eV at room temperature with the trion binding energy of ~100 meV.[14] Although the trion binding energy of BP is considerable, the weak ambient stability,

especially for monolayer or bilayer BP, limits its application in future trionic devices. More importantly, subject to the narrow bandgap, the PL emission of BP mainly lies in near-infrared range.

Violet phosphorus (VP), another allotrope of the elemental phosphorus, was firstly identified by W. Hittorf in 1865.[15] The subtle van der Waals (vdW) layered phosphorus bi-tubular structure leads to abundant exciton-related phenomena, *e.g.*, strong PL emissions in the visible range (from ~ 1.67 eV to ~ 2.50 eV) at room temperature.[16-20] Moreover, the thermal stability of VP is higher than that of BP, suggesting that VP and its low-dimensional counterparts are more promising candidates for the research of excitonic physics and optoelectronic applications.[17, 21, 22] Nevertheless, to the best of our knowledge, the trionic effect in VP have yet to be explored.

In this work, we synthesised layered VP crystals by the chemical vapor transport (CVT) method and subsequently studied the trionic effect of the mechanically exfoliated VP flakes comprehensively. We found that a robust T emission contributes to the PL spectra of the VP crystals with a huge trion binding energy of around 109 meV. Using a mild Ar^+ plasma post-treatment method, we observed a conversion from T emission to X^0 emission. Through X-ray photoelectron spectroscopy (XPS) and scanning transmission electron microscopy with high-angle annular dark field (STEM-HAADF) measurements, we confirm a combination of two effects leading to the T-to-X^0 conversion, *i.e.* the reduction of stannous Sn-I-P impurities accompanied with the surface defects-induced electron withdrawal. Furthermore, those surface defects can also enhance the photodetection of the VP phototransistors dramatically based on the hole-trapping mechanism. Our results pave the way for further investigating trionic effect and its promising applications in 2D optoelectronic devices.

2. Results and Discussion

Layered VP crystals were synthesized by the CVT method with the precursors of amorphous RP, tin (Sn), and iodine (I_2), where Sn and I_2 were used as the mineralization additives and active transport species, respectively.[23-25] The detailed synthesis process is given in the Experimental Section. **Figure 1**a shows the optical image of a mechanically exfoliated VP flake deposited onto a 285 nm SiO_2/Si^{++} substrate. Atomic force microscopy (AFM) gives the thickness of 54.9 nm. Similar to mechanically exfoliated BP flakes, visible droplets were found on the surface of the as-prepared VP flake, which is ascribed to the highly hydrophilic characteristic of elemental P.[26] However, unlike the orthorhombic structure of BP, VP belongs to the monoclinic structure with a space group of *P2/n* (No. 13),[17] and the atomic structure is more complicated than BP. Figure 1b illustrates the atomic structure of VP crystals.[27] Each unit cell of a VP crystal contains 21 atoms as labelled in the left-bottom of Figure 1b, which constitutes a phosphorus tube with a pentagonal cross-section as verified by the cross-sectional STEM-HAADF imaging shown in Figure 1c. One phosphorus tube consists of three sub-units, a P_9 cage and a P_8 cage as the building units connected by phosphorus dumbbells P_2.[18] The roof P_{21} atom covalently connects to another level of phosphorus tubes to make up a fundamental structure named the bi-tubular layer.[20] The connected two levels are cross-hatched, as shown in the left-top panel of Figure 1b. Those bi-tubular levels stack along the perpendicular direction *via* van der Waals (vdW) forces to form the bulk counterpart, as shown in the right panel of Figure 1b. Through the STEM-HAADF imaging, clear periodical lattice fringes were observed, suggesting the high crystalline quality of the synthesised VP crystal. The planar distance along the *c* direction between adjacent bi-tubular layers was measured as 2.223 nm close to the reported value

(2.189 nm).[17] The slight deviation may result from the different crystallinity in diverse synthesis processes.[28]

The Raman spectra were also collected from the exfoliated VP flake, excited by a 532 nm laser. As shown in Figure 1d, more Raman modes exist in the range below 600 cm^{-1} compared to BP and amorphous RP. The sophisticated Raman spectrum is attributed to the bi-tubular structure of VP, which reflects the low symmetry of atomic vibrations.[29] Following Fasol's work,[18] the phonon modes of VP can be classified into two groups coarsely: high frequency modes above ~350 cm^{-1} and low frequency modes below ~290 cm^{-1}. There is a forbidden gap between the two groups, which is not observed in BP/amorphous RP. In the high frequency range, major localised bond stretching and bond bending contribute to these intra-tube modes. For the modes in the low frequency range, bond stretching contributes little to these modes. Integral rotation of atoms, bond angle distortion, and vdW force significantly influence these inter-tube modes. The Raman modes below ~140 cm^{-1} are related to the inter-tube vibrations through the weak vdW restoring force. The complex Raman spectrum reflects the large density of phonon states in VP crystals, which further hints at a strong light-matter interaction and electron-phonon scattering.[30]

In order to investigate the trionic effect on the optical properties of VP crystals, Ar^+ plasma post-treatment was used to modify our as-prepared samples. **Figure 2**a shows the PL spectra of an exfoliated VP flake as a function of the Ar^+ plasma exposure time. A prominent PL peak is observed with the maximum intensity at ~ 657.1 nm (1.89 eV). Considering the large exciton binding energy in 2D confined systems, it is reasonable to assign the prominent PL emission to be the excitonic recombination. The PL emission energy is related to the optical bandgap and defined as the electronic

bandgap by subtracting the exciton binding energy.[4, 31] A step-by-step Ar^+ plasma exposure was implemented to investigate the influence on the PL emission. Notably, we did not use the oxygen plasma to minimise the unexpected influence of surface oxidation.[32, 33] During the whole 300 s Ar^+ plasma exposure, a visible snap blue-shift (~ 10 nm) of the PL peak position occurred in the initial 180 s stage. Then, only tiny successive PL shifts can be observed in the following 120 s stage. Similar phenomena of the snap blue-shift in the initial stage have also been observed in MoS_2, resulting from the removal of physically adsorbed H_2O/O_2 molecules or containments on the surface.[34] This kind of adsorption can be easily eliminated by the mild Ar^+ plasma etching, as verified by the AFM surface morphology measurement shown in Figure S4 (Supporting Information). The RMS roughness declines from 21.7 nm (as-prepared sample) to 8.7 nm (120 s exposure). Besides, in view of the subsequent tiny PL shift in the following stages, we deem that the thickness induced PL shift is limited in the initial 180 s stage. A detailed discussion is given in Section S1 (Supporting Information).

Notably, besides the snap blue-shift, a progressive variation in the line-shape of the PL spectra proportionate to the Ar^+ plasma exposure time is exhibited in the process until a steady state is reached after 300 s of treatment. The broad PL peak in the as-prepared sample gradually becomes narrow, as indicated by the black arrow in Figure 2a. Commonly, a broad PL spectrum reflects strong exciton-phonon scattering, which derives from the defects/impurities induced disorders.[35, 36] With the existences of defects/impurities in the VP crystals, unintentional doping would cause the neutral X^0 to capture excess electrons/holes to form negative/positive T. As shown in Figure 2b, the integrated PL spectra after different Ar^+ plasma treatment time can be well fitted by a dual-Gaussian function just by varying the spectral weights of two peak components. The prominent peak (the yellow one)

with the central wavelength at ~ 647 nm is from the X^0 emission, while the right shoulder (the purple one) with a peak position at ~ 713 nm is ascribed to the T emission. As the Ar^+ plasma exposure time increases, the T emission peak becomes gradually less intense until reaching a steady state after 300 s treatment. The fitted curve areas (spectral weights) represent the population of X^0 and T associated with electron densities.[10, 37] We found that the PL spectral weights of the X^0 and T emissions gradually changes from X^0: 70.5 %, T: 29.5 % in the as-prepared sample to X^0: 96.1 %, T: 3.9 % in the 300 s plasma-treated one as shown in Figure 2c, suggesting a gradual decline of the T population. Moreover, compared with the almost unchanged X^0 peak energy, the T peak energy shows a slight decrease (~ 20 meV) in the etching process. This phenomenon is ascribed to the Fermi level shift in the treated sample.[38] As is known, their peak energy difference ($\Delta\hbar\omega$) is defined as the trion dissociation energy equal to the sum of trion binding energy (E_{Tb}) and the energy needed to recoil the unbound electron to the Fermi level ($d'E_F$),

$$\triangle \hbar\omega = E_{Tb} + d'E_F \qquad (1)$$

where $d'$is a constant.[39] The trion dissociation energy determines the upper limit of the trion binding energy, which will be analyzed in detail in the following. Gate-tunable PL emission is a common method to modulate the T population through the electrostatic doping.[8, 13] Figure 2d illustrates that the evolution of PL spectra as a function of the applied back-gate voltage based on a metal-insulator-semiconductor (MIS) structure. As shown in the inset of Figure 2d, mechanical exfoliated graphene (Gr) was employed as the bottom electrode covered by a layer of thin hexagonal boron nitride (h-BN) as an effective insulator. When a back-gate voltage of +80 V is applied to the Gr electrode, the PL spectrum of the VP flake exhibits obvious two peaks located at ~ 668 nm (X^0

emission) and ~ 741 nm (T emission), respectively. Notably, the intensity of X^0 emission is highly dependent on the applied back-gate voltage. As the back-gate voltage sweeps from positive to negative, more electrons are extracted from the n-type VP flake leading to the enhancement of X^0 emission. Notice that the reason of n-type will be discussed later. In contrast, the intensity of T emission is weakly dependent on the applied voltage as shown in Figure S7. Similar trends are also observed in the gate-tunable PL emission of other 2D materials, which can be used as the criteria of trions.[40]

Temperature dependence of the PL spectra was performed to investigate the excitonic bound states of the layered VP crystal and further confirms the assignment of the X^0 and T peak components. **Figure 3**a shows the temperature-dependent evolution of the PL spectra under a 532 nm laser excitation. At high temperature (273 K), obvious X^0 and T peak components can be observed with a larger spectral weight of X^0 emission, indicating the lower thermal stability of T in VP crystals, which has been verified in BP and MoS_2.[41, 42] As the temperature decreases to liquid nitrogen temperature (77 K), both the X^0 and T emissions become more intense, which is ascribed to the reduced phonon scattering at low temperature.[43] Also, clear blue-shifts of the peak positions indicated by the black arrows are found for both X^0 and T emissions. Figure 3b shows the peak emission energy of X^0 and T extracted by the dual-Gaussian fitting. The blue-shifts of the emission energy are in accordance with the Varshni equation, which describes the temperature-dependent bandgap of semiconductors based on the electron-phonon coupling,[44, 45]

$$E_g(T) = E_g(0) - S\hbar\omega[coth(\frac{\hbar\omega}{2kT}) - 1] \quad (2)$$

where $E_g(0)$ is the ground-state transition energy at 0 K, *S* is a dimensionless coupling constant and $\hbar\omega$ is an average phonon's energy.[46] Based on the fitting lines of X^0 and T, we found that the X^0 (T) emission energy is located at 1.91 eV (1.80 eV) with the trion dissociation energy ($\triangle \hbar\omega$) of ~ 110 meV at 77 K. When the temperature increases gradually, the dissociation energy increases to ~ 160 meV at 273 K. Though the intensities of both X^0 and T emissions become larger at low temperatures, the relative spectral weight of T emission gradually increases as the temperature decreases. In Figure 3c, the ratio of the spectral weight of T /X^0 changes from 0.17 at 273 K to 0.75 at 77 K. The significant increase of the T spectral weight demonstrates that more T are formed at low temperature. As is known, the phonon scattering is strongly weakened at low temperature due to the suppression of the lattice vibrations. And, the impurities-related emission processes dominate the electron-hole pairs' recombination. With impurities in the VP crystals, negative T are formed by capturing the doped electrons. Thus, a strong T emission can be observed at low temperatures, which has also been found in other 2D materials.[45, 47] By applying the mass action model, we fitted the spectral weight ratio of T/X^0 as a function of temperature well with a specified trion binding energy (E_{Tb}).[48] Detailed methods are discussed in Section S2 (Supporting Information). In 2D systems, the Fermi level is relative to the carrier density ($E_F = \hbar^2\pi n_e/2m_e e^2$), where n_e is the carrier density and m_e is the effective electron mass.[8] Given the definition of trion binding energy (Equation 1), we were able to plot linearly the $\triangle \hbar\omega$ as a function of carrier density (n_e) with an intercept of ~108.9 meV, as shown in Figure 3d. When a VP crystal lies in a charge-neutral state, the trion dissociation energy is equal to E_{Tb}. Therefore, we could determine E_{Tb} the of the VP crystal ($E_{Tb} \approx 109$ meV), which is relatively larger among common layered materials. Table S1 (Supporting Information) shows the E_{Tb}

of common 2D materials for comparisons. Besides the temperature-dependent X^0 and T emissions, laser power-dependent PL spectra also confirm the assignment of X^0 and T peak components as illustrated in Figure S8 (Supporting Information). As the incident laser power increases, more photogenerated carriers are injected to enhance the screening effect, resulting in neglecting the influence of the initial doping level ($d'E_F$). Since the initial doping level determines the density of the free carriers, the T population is limited, which leads to a saturation of the T emission intensity. A similar phenomenon has also been observed in BP.[14]

It is essential to investigate the composition of the VP crystals to reveal the underlying mechanism of the T emission. XPS was employed to characterize the valence state of P and the possible chemical states. Noticeably, all XPS data were calibrated by the C (*1s*) peak 284.8 eV in our work. As shown in **Figure 4**a, the XPS spectra of P *2p* core can be resolved into twin peaks centred at 129.7 eV ($2p_{3/2}$) and 130.5 eV ($2p_{1/2}$) with a spin-orbit splitting difference of ~ 0.8 eV as determined by a Gaussian line-shape fitting. Our data match well with the reported results of elemental P^0.[49] Additionally, a broad peak envelope exists in the binding energy's (BE) range from 132.5 eV to 135.7 eV, corresponding to the phosphorus oxidized species with multiple P-O and P=O bonding states.[50] So, we assigned the peak as PO_x, mainly including phosphorus pentoxide (P_4O_{10}) with a higher BE centred at 134.9 eV and phosphorus oxides with lower-oxidation states (P < +5), such as phosphorus trioxide (P_4O_6). Simultaneously, the O 1s peak can be deconvoluted into three components with centers at 531.8 eV, 532.9 eV and 533.8 eV, as shown in Figure 4b, respectively. The dominant peak component (532.9 eV) is ascribed to the SiO_2 substrate. The lower BE component (531.8 eV) and the higher one (533.8 eV) result from the dangling (P=O) and bridging (P-O-P) oxygen, respectively.[51]

Moreover, as surface phosphorus oxides readily react with H_2O to form phosphoric acid-like species, adsorbed H_2O molecules may also contribute to the higher BE components in the O *1s* peak.[52] The existence of both P *2p* peak at 134.9 eV and O *1s* at 531.8 eV and 533.8 eV is a signature for phosphorus pentoxide.[53] So far, we are almost certain to conclude those phosphorus oxides formed by the chemically adsorbed H_2O/O_2 on the surface of the as-prepared VP flake. The phosphorus oxides can withdraw the free electrons from the VP crystals,[34] leading to an electron depletion layer near the surface and facilitating partial T to convert into X^0 in the n-type as-prepared VP crystals.

After 220 s Ar^+ plasma treatment in the same recipe (~19 nm in-depth), the peak positions of the P^0 remain almost unchanged, with a mild reduction of the peak intensity reflecting the volume reduction. However, we found that the PO_x peak envelope made a slight shift toward the lower binding energy, which is ascribed to the clean effect of the Ar^+ plasma. Interestingly, the relative peak intensity of P_4O_{10} increases significantly, implying that there are more phosphorus oxides with high oxidized states after the Ar^+ plasma treatment. This phenomenon can also be verified by the variation of O *1s* peak in the treated sample. P_4O_{10} possesses both the dangling (P=O) bonds and the bridging (P-O-P) bonds, while P_4O_6 is mainly formed with the bridging ones.[54] Apparently, the relative peak area ratio of (P=O) /(P-O-P) changes from 0.97 to 2.51 after the Ar^+ plasma treatment. It suggests that Ar^+ plasma treatment can not only clean the surface but also introduce more dangling bonds on the surface of the residues. These plasma-induced dangling bonds can serve as surface defects and active centres for more H_2O/O_2 molecules adsorption.[55] So, it is still observed the existence of PO_x on the surface after the Ar^+ plasma treatment. In short, it could be understood as follows: the as-prepared VP crystals are n-type doped with a high density of equilibrium free electrons, which results

in strong T emissions in the initial state. After the Ar^+ plasma exposure, though the native phosphorus oxides on the surface are removed, more dangling bonds are introduced and chemically adsorb more H_2O/O_2 to form phosphorus pentoxides-like species, which further depletes the free electrons and leads to the suppression of T emissions.

To understand the intrinsic n-type of the as-prepared VP crystal, we also measured the XPS spectra of elemental Sn and I, as shown in Figure 4c, d. The lower panel of Figure 4c shows the Sn *3d* core level of the as-prepared sample. A clear *3d 5/2* peak is located at 487.4 eV, corresponding to Sn^{4+} state.[56] Moreover, besides the chemically bound elemental Sn, a weak shoulder peak is located at 485.3 eV, assigned to Sn metal (Sn^0).[57] Given the melting point of metal Sn (231.9 ℃), it is reasonable that parts of Sn metal adhere to the exterior of the crystals, which can be confirmed by the FE-SEM (field emission scanning electron microscopy) – energy dispersive X-ray spectroscopy (EDS) measurements shown in Figure S9 (Supporting Information). Unlike the elemental Sn, the melting point of I is only 113.6 °C, and the boiling point is 185.2 °C. The gaseous iodine deposited onto the VP crystals' surface was fairly limited due to the volatility. Therefore, it is found that the I *3d 5/2* peak intensity is weaker than that of Sn, as shown in Figure 4d. The broad I *3d 5/2* peak can be resolved into two components located at 618.4 eV (iodine ions, I^-) and 619.6 eV (elemental iodine, I^0).[58] Those results indicate that most iodides (~ 84%) are physically deposited or adhered to the exterior of the as-prepared VP crystals. So, stannic species with Sn^{4+} state on the surface can donate excess electrons to VP crystals and O_2 molecules due to the weak electronegativity of metal.

After the Ar^+ plasma exposure, a visible Sn *3d* peak is still observed with a shift toward lower BE (~ 0.6 eV), which suggests that there is still Sn in the interior with a stannous Sn^{2+} state. Moreover,

the small shoulder peak (~ 128.3 eV) in the P *2p* region as shown in the upper panel of Figure 4a is assigned to the metal phosphide, *i.e.* the Sn-P bonds, demonstrating that stannous Sn-P compounds underlie the pristine surface, which is also confirmed by the disappearance of the Sn^0 peak in the Sn *3d* core-level spectrum after the Ar^+ plasma treatment. Given elemental I, the integrated BE spectral area of elemental I strongly increase by ~4 times after the treatment. Especially, the I^- component increases significantly. Therefore, based on the composition analysis, the stannous Sn-I-P compounds should exist in the interior of the VP crystals, which serves as the electron donors leading to the intrinsic n-type characteristic. Besides of the XPS chemical state analysis, cross-sectional STEM-HAADF with atomic resolved EDS mapping visually confirms that the stannous Sn-I-P compounds are incorporated into the VP lattices dispersedly as represented by the bright spots. The details are given in Section S3 (Supporting Information). The Ar^+ plasma treatment can remove the stannous Sn-I-P inclusions accompanied by the decrease of the sample thickness, which efficiently suppresses the intrinsic n-type doping. Therefore, the Ar^+ plasma treatment can result in a combined effect, which leads to the T to X^0 conversion in the process. One is removing the stannous Sn-I-P compounds as the n-type dopants embedded into the lattice; The other is withdrawing the free electron by the phosphorus oxidized species at the outer surface,

Given the robust trionic effect in the layered VP crystals, VP phototransistors based on the classical field-effect transistor (FET) structure were fabricated to explore its promising optoelectronic applications. **Figure 5**a shows the schematic diagram of a VP phototransistor under illumination. The channel thickness is around 30 nm, as shown in Figure S12 (Supporting Information). Because of the spontaneous oxidation and physically adsorbed H_2O/O_2 on the top surface of the VP crystals, the

intrinsic equilibrium free electrons are extracted from the n-type VP crystal, which leaves behind an electron depletion region with the potential direction towards the top surface. Upon illumination, photogenerated holes migrate along the potential slope and are trapped near the negatively charged surface defects, which serves as hole-trap centers on the surface.[59] The band diagram inset of Figure 5a illustrates the hole-trapping mechanism through the surface defects can boost the high density of hole-trap states due to the dangling bonds on the surface and enhance the photodetection.[59] Figure 5b shows the transfer curves of a VP phototransistor at room temperature. A predominated electron branch is observed in dark condition further confirming the intrinsic n-type doping by the stannous Sn-I-P impurities. Once illuminated, the transfer curves exhibit more severe n-type characteristics governed by the aforementioned hole-trapping mechanism. Moreover, the I-V curves in the inset show a distinct augment of the photoconductance (~ 35.5 pS) under the 532 nm laser illumination. Photogenerated hole trapping would be easier if excited by higher energy photons. These hot holes are more energetic and delocalized in the sample and readily migrate to the localized surface traps, which results in more unpaired electrons and a larger photoconductance.

Figure 5c depicts the photocurrent dependence on the drain voltage (V_d) illuminated with different wavelengths and under dark condition. No visible photocurrent saturation in the I-V curves implies that the influence of the Schottky barriers is negligible and that the Fermi level of the VP channel lies close to the conduction band when no gate bias (V_g) is applied. By calculating the responsivity $R = (I_{illu} - I_{dark})/P_{in} \cdot S$, where I_{illu} and I_{dark} are the measured current in illumination and dark condition, respectively, P_{in} is the incident-light intensity, S is the effective illuminated area, the highest responsivity (~ 0.15 mA/W) is obtained at around 452 nm as shown in the inset.[60] Obviously,

an onset of photoresponse is found at around 650 nm related to the optical bandgap of the VP crystals, matching well the obtained PL spectrum.

To confirm the surface-defects related photodetection enhancement, another thicker VP (~ 207 nm) phototransistor was prepared in order to weaken the influence of the reduction of channel thickness. After 120 s Ar^+ plasma treatment, the photoconductance increases greatly by 5.4 times (inset) with a more obvious n-type transfer characteristic as shown in Figure 5d. As mentioned above, more surface defects are introduced after the plasma treatment to form hole-trap centers. With that assistance, more unpaired photo-generated electrons contribute to the increase of photocurrent resulting in the visible electron conductance in the treated VP phototransistor. Correspondingly, the values of R at all excitation wavelengths are increased with the maximum increment by 8.5 times for the 452 nm excitation as illustrated in Figure 5e. Finally, the temporal photoresponse response to the influence of Ar^+ plasma treatment is shown in Figure 5f, where the device was under a 445 nm laser diode illumination with V_d = 0.5 V, V_g = 0 V. The current periodically changes with the alternate on-off switching of the laser, suggesting a highly stable and reversible response of the VP phototransistor. Benefiting from the surface defects-induced hole trapping, the value of photocurrent switching on/off ratio (I_{on} / I_{off}) increases by around 2 times after the Ar^+ plasma treatment. Moreover, it is found that the photocurrent takes more time to stabilize in the treated phototransistor, which confirms in turn that more surface defects exist on the VP surface after the Ar^+ plasma treatment.

3. Conclusions

In summary, layered VP crystals have been synthesised by a CVT method with an amorphous RP/Sn/I_2 system as precursors. Mechanically exfoliated VP flakes show an intense broad PL spectrum with robust T emission at room temperature. By adjusting the Ar^+ plasma exposure time, the variation of relative spectral weights of the X^0 and T emissions demonstrates a conversion from T to X^0. The trion binding energy was estimated to be around 109 meV, much larger than other common layered materials. Combined with the XPS and STEM-HAADF results, it is found that stannous Sn-I-P impurities are incorporated into the VP lattices serving as electron donors and facilitate the T formation. We propose that a combination of two factors results in the T-to-X^0 conversion, *i.e.* one is the decline of stannous Sn-I-P impurities' population after the Ar^+ plasma treatment; the other is the electron withdrawal induced by the phosphorus oxidized species in the surface regions. Furthermore, the phosphorus oxidized species are conducive to the photodetection enhancement based on the hole-trapping mechanism. In a word, our results reveal that the layered VP crystal is a kind of promising material for both the basic study of excitonic physics and future trionic devices at the 2D limit.

4. Experimental Section

Growth of violet phosphorus: VP crystals were synthesized by the CVT method with the precursors of amorphous red phosphorus (400 mg, ≥97 %), granular iodine (25 mg, 99.8 %) and tin (35 mg, 99.995 %). The precursors were sealed in an evacuated ampoule and heated by a tube furnace, as shown in Figure S1 (Supporting Information). The corresponding temperature ramping profile is shown in Figure S2 (Supporting Information).

Ar^+ plasma exposure of violet phosphorus flake: A ceramic mortar was used to mash the reddish-brown as-synthesised VP crystals with by-products. Then, mechanical exfoliation was used to deposit the VP flakes onto 285 nm SiO_2/Si^{++} substrates with the mashed powder as the exfoliation source. Subsequently, the as-prepared VP flakes were treated with Ar^+ plasma etching by using a TRION ICP-RIE system. The Ar^+ plasma was generated in a mild recipe with 30 sccm argon flow at 10 mTorr pressure. The ICP and RIE power was set to 250 W and 40 W, respectively. The etching rate can be controlled to be ~ 0.09 nm/s, as shown in Figure S5 (Supporting Information).

Optical measurement: Both PL and Raman measurements were conducted on a Witech alpha 300R confocal micro-Raman system excited by a 532 nm continuous-wave laser. Typically, the laser power was set as no larger than 0.5 mW without a particular statement in case the heating-induced degradation. A Linkam HFS350EV stage was used for gate-tunable and temperature-dependent PL measurement. Typically, the integration time of the PL measurement was set to be 0.5 s.

Characterization: An atomic force microscope (Veeco Multimode 8) was used to identify the thickness of the layered VP in tapping mode and at ambient conditions. The X-ray diffraction (XRD) spectrum was conducted on the Rigaku Smartlab and is shown in Figure S3 (Supporting Information). FE-SEM measurements were carried out on TESCAN MAMIA3 equipped with an Oxford EDS detector. The XPS was conducted on a Thermo Scientific NEXSA XPS system with a 12 kV Al Kα X-ray source. The spot size was minimized to a circle with a 70 μm diameter. The VP specimens for cross-sectional STEM were prepared by a dual-beam focused ion beam (FIB) nanofabrication platform (Helios 600i, Thermofisher). A Pt protection layer was first deposited on the top surface, followed by etching the surrounding area to form the sample lamella using a 30 kV accelerating

voltage gallium ion beam. The sample lamella observation area was then thinned to less than 100 nm thickness, and amorphous surface damage layers were polished with a 2 kV low energy gallium beam. The atom-resolved STEM-HAADF characterization was acquired on a Thermofisher Titan G2 60-300 aberration-corrected S/TEM microscope with an accelerating voltage of 300 kV. The probe convergence angle was 25 mrad, and the angular range of the HAADF detector was from 79.5 to 200 mrad. A Bruker Super-X EDS 4 detector system was used for STEM-EDS acquisition.

Fabrication of VP phototransistors: Standard electron beam lithography was employed to pattern electron-beam evaporated Cr/Au (5/60 nm) electrodes for VP phototransistors. The illuminated transfer characteristics and the time-dependent photocurrents were measured by using laser diodes as the illumination source. The wavelength-dependent photocurrents were excited by a 300 W xenon lamp filtered by various ultra-narrow bandpass filters. The transparent efficiency of these filters can reach ~ 90% with the full bandwidth at half maximums of 10 nm. The electrical measurements were carried out in a vacuum chamber using a Lakeshore probe station with a Keithley 4200 semiconductor parameter analyzer.

Supporting Information

Supporting Information is available from the Wiley Online Library or from the author.

Acknowledgement

This work was financially supported by the Hong Kong Polytechnic University (PolyU) grant (1-ZVGH) and the Research Grants Council of Hong Kong (Project nos. PolyU 153039/17P and

5303219). S.H.C. acknowledges the support of startup grants (P0035826) from the Department of Applied Physics, the Hong Kong Polytechnic University and the open subject of National Laboratory of Solid State Microstructures, Nanjing University (M34001).

Conflict of Interest

The authors declare no conflict of interest.

References

[1] G. Eda, H. Yamaguchi, D. Voiry, T. Fujita, M. Chen, M. Chhowalla, *Nano Lett.* **2011**, *11*, 5111.

[2] A. Splendiani, L. Sun, Y. Zhang, T. Li, J. Kim, C. Y. Chim, G. Galli, F. Wang, *Nano Lett.* **2010**, *10*, 1271.

[3] J. Wang, F. Lin, I. Verzhbitskiy, K. Watanabe, T. Taniguchi, J. Martin, G. Eda, *Nano Lett.* **2019**, *19*, 7470.

[4] M. M. Ugeda, A. J. Bradley, S. Shi, F. H. da Jornada, Y. Zhang, D. Y. Qiu, W. Ruan, S. Mo, Z. Hussain, Z. Shen, F. Wang, S. G. Louie, M. F. Crommie, *Nat. Mater.* **2014**, *13*, 1091.

[5] A. Chernikov, T. C. Berkelbach, H. M. Hill, A. Rigosi, Y. Li, O. B. Aslan, D. R. Reichman, M. S. Hybertsen, T. F. Heinz, *Phys. Rev. Lett.* **2014**, *113*, 076802.

[6] H. R. Gutierrez, N. Perea-Lopez, A. L. Elias, A. Berkdemir, B. Wang, R. Lv, F. Lopez-Urias, V. H. Crespi, H. Terrones, M. Terrones, *Nano Lett.* **2013**, *13*, 3447.

[7] K. He, N. Kumar, L. Zhao, Z. Wang, K. F. Mak, H. Zhao, J. Shan, *Phys. Rev. Lett.* **2014**, *113*, 026803.

[8] K. F. Mak, K. He, C. Lee, G. H. Lee, J. Hone, T. F. Heinz, J. Shan, *Nat. Mater.* **2013**, *12*, 207.

[9] J. S. Ross, S. Wu, H. Yu, N. J. Ghimire, A. M. Jones, G. Aivazian, J. Yan, D. G. Mandrus, D. Xiao, W. Yao, X. Xu, *Nat. Commun.* **2013**, *4*, 1474.

[10] S. Mouri, Y. Miyauchi, K. Matsuda, *Nano Lett.* **2013**, *13*, 5944.

[11] J. D. Lin, C. Han, F. Wang, R. Wang, D. Xiang, S. Qin, X.-A. Zhang, L. Wang, H. Zhang, A. T. S. Wee, W. Chen, *ACS Nano* **2014**, *8*, 5323.

[12] J. Jadczak, A. Delgado, L. Bryja, Y. S. Huang, P. Hawrylak, *Phys. Rev. B* **2017**, *95*, 195427.

[13] R. Xu, S. Zhang, F. Wang, J. Yang, Z. Wang, J. Pei, Y. W. Myint, B. Xing, Z. Yu, L. Fu, Q. Qin, Y. Lu, *ACS Nano* **2016**, *10*, 2046.

[14] J. Yang, R. Xu, J. Pei, Y. W. Myint, F. Wang, Z. Wang, S. Zhang, Z. Yu, Y. Lu, *Light Sci. Appl.* **2015**, *4*, e312.

[15] W. Hittorf, *Annalen der Physik Und Chemie* **1865**, *202*, 193.

[16] F. Baumer, Y. Ma, C. Shen, A. Zhang, L. Chen, Y. Liu, D. Pfister, T. Nilges, C. Zhou, *ACS Nano* **2017**, *11*, 4105.

[17] L. Zhang, H. Huang, B. Zhang, M. Gu, D. Zhao, X. Zhao, L. Li, J. Zhou, K. Wu, Y. Cheng, J. Zhang, *Angew. Chem. Int. Ed.* **2020**, *59*, 1074.

[18] G. Fasol, M. Cardona, W. Honle, H. G. v. Schnering, *Solid State Commun.* **1984**, *52*, 307.

[19] C. G. Michel, R. Schachter, M. A. Kuck, J. A. Baumann, P. M. Raccah (Stauffer Chemical Company), *US Patent 1986, 4620968*.

[20] G. Schusteritsch, M. Uhrin, C. J. Pickard, *Nano Lett.* **2016**, *16*, 2975.

[21] S. Lin, W. K. Lai, Y. Li, W. Lu, G. Bai, S. P. Lau, *SmartMat* **2021**, *2*, 226.

[22] A. Fali, M. Snure, Y. Abate, *Appl. Phys. Lett.* **2021**, *118*, 163105.

[23] M. Zhao, X. Niu, L. Guan, H. Qian, W. Wang, J. Sha, Y. Wang, *CrystEngComm* **2016**, *18*, 7737.

[24] M. Köpf, N. Eckstein, D. Pfister, C. Grotz, I. Krüger, M. Greiwe, T. Hansen, H. Kohlmann, T. Nilges, *J. Cryst. Growth* **2014**, *405*, 6.

[25] L. Zhang, M. Gu, L. Li, X. Zhao, C. Fu, T. Liu, X. Xu, Y. Cheng, J. Zhang, *Chem. Mater.* **2020**, *32*, 7363.

[26] A. Castellanos-Gomez, L. Vicarelli, E. Prada, J. O. Island, K. L. Narasimha Acharya, S. I. Blanter, D. J. Groenendijk, M. Buscema, G. A. Steele, J. V. Alvarez, H. W. Zandbergen, J. J. Palacios, H. S. J. van der Zant, *2D Mater.* **2014**, *1*, 025001.

[27] V. H.Thurn, H. Kerbs, *Acta Cryst. B* **1969**, *B25*, 125.

[28] I. C. Bassignana, D. A. Macquistan, G. C. Hillier, R. Streater, D. Beckett, A. Majeed, C. Miner, *J. Cryst. Growth* **1997**, *178*, 445.

[29] L. Zhang, H. Huang, Z. Lv, L. Li, M. Gu, X. Zhao, B. Zhang, Y. Cheng, J. Zhang, *ACS Appl. Electron. Mater.* **2021**, *3*, 1043.

[30] D. J. Olego, J. A. Baumann, M. A. Kuck, R. Schachter, C. G. Michel, *Solid State Commun.* **1984**, *52*, 311.

[31] F. Cadiz, E. Courtade, C. Robert, G. Wang, Y. Shen, H. Cai, T. Taniguchi, K. Watanabe, H. Carrere, D. Lagarde, M. Manca, T. Amand, P. Renucci, S. Tongay, X. Marie, B. Urbaszek, *Phys. Rev. X* **2017**, *7*, 021026.

[32] Y. Liu, H. Nan, X. Wu, W. Pan, W. Wang, J. Bai, W. Zhao, L. Sun, X. Wang, Z. Ni, *ACS Nano* **2013**, *7*, 4202.

[33] J. Jia, S. K. Jang, S. Lai, J. Xu, Y. J. Choi, J.-H. Park, S. Lee, *ACS Nano* **2015**, *9*, 8729.

[34] S. Tongay, J. Zhou, C. Ataca, J. Liu, J. S. Kang, T. S. Matthews, L. You, J. Li, J. C. Grossman, J. Wu, *Nano Lett.* **2013**, *13*, 2831.

[35] A. Surrente, A. A. Mitioglu, K. Galkowski, W. Tabis, D. K. Maude, P. Plochocka, *Phys. Rev. B* **2016**, *93*, 121405(R).

[36] O. A. Ajayi, J. V. Ardelean, G. D. Shepard, J. Wang, A. Antony, T. Taniguchi, K. Watanabe, T. F. Heinz, S. Strauf, X. Y. Zhu, J. C. Hone, *2D Mater.* **2017**, *4*, 031011.

[37] J. Zhang, L. Ding, S. Zhou, Y. M. Xiao, W. Xu, *Phys. Status Solidi-R* **2020**, *14*, 2000222.

[38] Y. K. Lin, R. S. Chen, T. C. Chou, Y. H. Lee, Y. F. Chen, K. H. Chen, L. C. Chen, *ACS Appl. Mater. Inter.* **2016**, *8*, 22637.

[39] Y. Kim, Y. I. Jhon, J. Park, C. Kim, S. Lee, Y. M. Jhon, *Sci. Rep.* **2016**, *6*, 21405.

[40] G. Plechinger, P. Nagler, J. Kraus, N. Paradiso, C. Strunk, C. Schüller, T. Korn, *Phys. Status Solidi-R* **2015**, *9*, 457.

[41] G. Zhang, A. Chaves, S. Huang, F. Wang, Q. Xing, T. Low, H. Yan, *Sci. Adv.* **2018**, *4*, eaap9977.

[42] M. Florian, M. Hartmann, A. Steinhoff, J. Klein, A. W. Holleitner, J. J. Finley, T. O. Wehling, M. Kaniber, C. Gies, *Nano Lett.* **2018**, *18*, 2725.

[43] S. Sharma, S. Bhagat, J. Singh, M. Ahmad, S. Sharma, *J. Mater. Sci.: Mater. Electron.* **2018**, *29*, 20064.

[44] Y. P. Varshni, *Physica* **1967**, *34*, 149.

[45] A. A. Mitioglu, P. Plochocka, J. N. Jadczak, W. Escoffier, G. L. J. A. Rikken, L. Kulyuk, D. K. Maude, *Phys. Rev. B* **2013**, *88*, 245403.

[46] S. Golovynskyi, I. Irfan, M. Bosi, L. Seravalli, O. I. Datsenko, I. Golovynska, B. Li, D. Lin, J. Qu, *Appl. Surf. Sci.* **2020**, *515*, 146033.

[47] J. W. Christopher, B. B. Goldberg, A. K. Swan, *Sci. Rep.* **2017**, *7*, 14062.

[48] N. Peimyoo, W. Yang, J. Shang, X. Shen, Y. Wang, T. Yu, *ACS Nano* **2014**, *8*, 11320.

[49] A. Thøgersen, M. Syre, B. Retterstol Olaisen, S. Diplas, *J. Appl. Phys.* **2013**, *113*, 044307.

[50] H. Zhu, S. McDonnell, X. Qin, A. Azcatl, L. Cheng, R. Addou, J. Kim, P. D. Ye, R. M. Wallace, *ACS Appl. Mater. Inter.* **2015**, *7*, 13038.

[51] H. Kwon, S. W. Seo, T. G. Kim, E. S. Lee, P. T. Lanh, S. Yang, S. Ryu, J. W. Kim, *ACS Nano* **2016**, *10*, 8723.

[52] A. Verdaguer, C. Weis, G. Oncins, G. Ketteler, H. Bluhm, M. Salmeron, *Langmuir* **2007**, *23*, 9699.

[53] Z. Mao, S. Dong, J. Li, X. Lin, X. Jian, P. Wu, *Solid State Commun.* **2020**, *314-315*, 113928.

[54] S. Wu, F. He, G. Xie, Z. Bian, J. Luo, S. Wen, *Nano Lett.* **2018**, *18*, 5618.

[55] H. Nan, Z. Wang, W. Wang, Z. Liang, Y. Lu, Q. Chen, D. He, P. Tan, Feng Miao, X. Wang, J. Wang, Z. Ni, *ACS Nano* **2014**, *8*, 5738.

[56] A. P. Xian, G. L. Gong, *J. Electron. Mater.* **2007**, *36*, 1669.

[57] J. F. Moulder, J. Chastain, *Handbook of X-ray Photoelectron Spectroscopy: A Reference Book of Standard Spectra for Identification and Interpretation of XPS Data*, Physical Electronics Division, Perkin-Elmer Corporation, Eden Prairie 1992.

[58] J. Kang, T. G. Levitskaia, S. Park, J. Kim, T. Varga, W. Um, *Chem. Eng. J.* **2020**, *380*, 122408.

[59] C. Soci, A. Zhang, B. Xiang, S. A. Dayeh, D. P. R. Aplin, J. Park, X. Y. Bao, Y. H. Lo, D. Wang, *Nano Lett.* **2007**, *7*, 1003.

[60] F. H. Koppens, T. Mueller, P. Avouris, A. C. Ferrari, M. S. Vitiello, M. Polini, *Nat. Nanotechnol.* **2014**, *9*, 780.

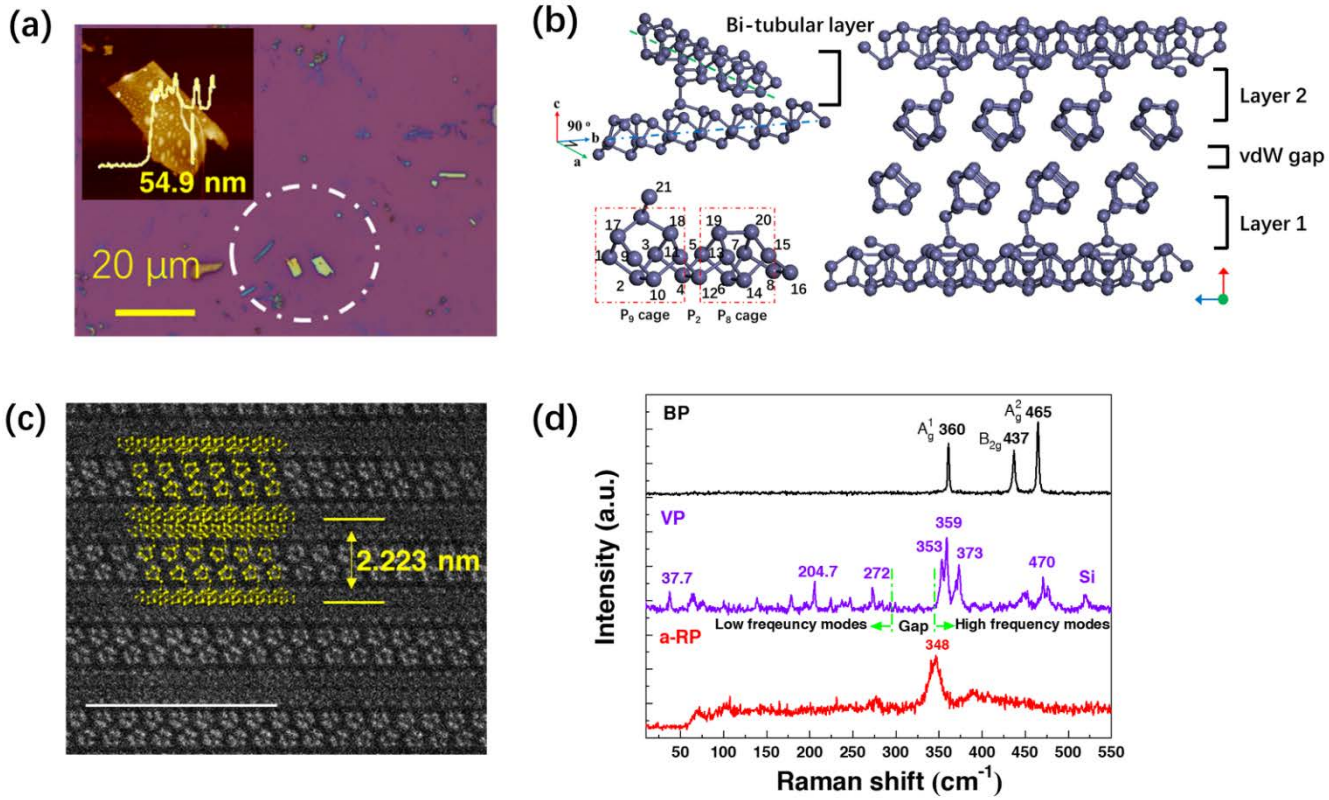

Figure 1. Atomic structure of the VP crystal and characterization. (a) Optical photo of a mechanically exfoliated VP flake highlighted by a white dash-dot circle on a 285 nm SiO_2/Si^{++} substrate. The inset AFM profile demonstrates the height is around 55 nm. (b) Schematic representation of the pentagonal tubular structure of VP. The bottom-left panel shows the unit cell consisting of a P_8 cage, a P_9 cage and a P_2 dumbbell. A pentagonal tubular is formed by the periodical extension of the unit cell. Through covalent bonding of the P21 atom, two tubes with vertical axial directions make up a bi-tubular layer, as shown in the top-left panel. Two bi-tubular layers stack along the *c* direction to form the layered VP crystal through vdW forces, as shown in the right panel. (c) Cross-sectional STEM-HAADF image of a VP flake with the atomic arrangement represented by the yellow ball-stick models. The scale bar is 5 nm. (d) Raman spectrum of a VP flake excited by a 532 nm laser compared to BP and amorphous RP.

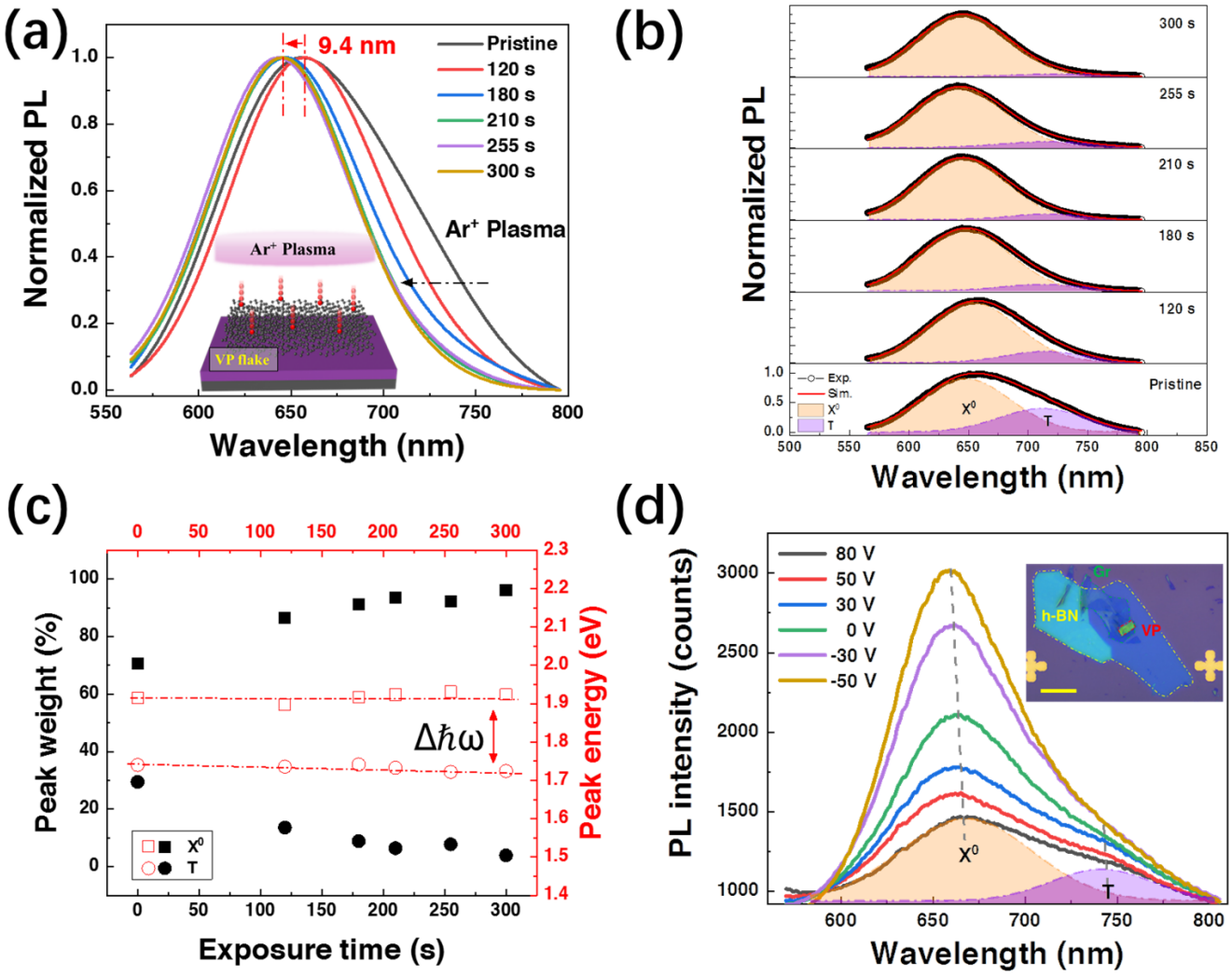

Figure 2. Evolution of X^0 and T emissions corresponding to an Ar^+ plasma treatment. **(**a) Normalized PL of a VP flake corresponding to the Ar^+ plasma exposure time. Inset is the schematic illustration of the Ar^+ plasma exposure process. (b) PL peak deconvolution against various Ar^+ plasma exposure times. The yellow (purple) peak component represents the X^0 (T) emission. The red solid lines are the dual-Gaussian fittings of the integrated PL spectra. (c) Spectral weight (black) and peak energy (red) of the X^0 (square) and T (circle) emissions as a function of the Ar^+ plasma exposure time. The dash dot lines are linear fittings of the extracted peak energy of X^0 and T emissions with a trion dissociation energy of $\hbar\omega$. (d) PL intensities of X^0 and T as a function of the back-gate voltages

from a metal-insulator-semiconductor (MIS) structure. The inset photo shows the MIS structure with graphene (green dashed area), h-BN (yellow dashed area) and VP (red dashed area) as the bottom electrode, intermediate insulator and semiconductor, respectively. The scale bar is 20 μm.

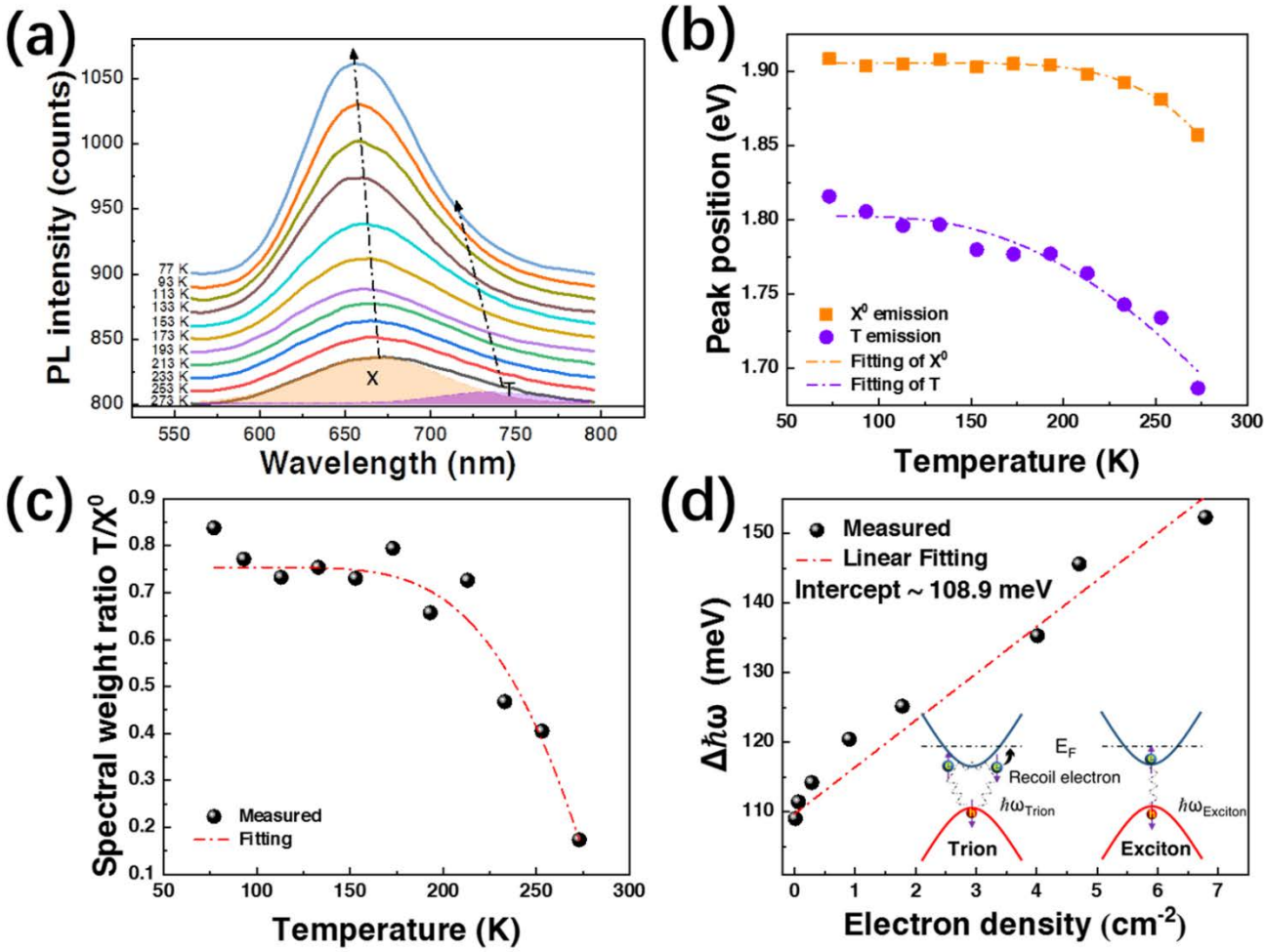

Figure 3. Evolution of X^0 and T emissions as a function of temperature and the calculation of trion binding energy. (a) Temperature-dependent evolution of the X^0 and T emissions. A representative deconvolution of the X^0 (yellow) and T (purple) emission components is illustrated in the case of 273 K. The black dash-dot arrows indicate the shifts of the X^0 and T peak positions. (b) The extracted peak energy of the X^0 and T emissions as a function of the temperature. The dash dot lines are fittings using Equation (2). (c) Spectral weight ratio of T/X^0 versus temperature with mass action model fitting (red dash-dot line). (d) The peak energy difference of the X^0 and T emissions as a function of the electron density. The red dash dot line is a linear fitting based on Equation (1) with an intercept

of ~108.9 meV, which determines the trion binding energy of VP. The inset depicts the trion dissociation into a neutral exciton accompanied by a recoil electron into the Fermi level.

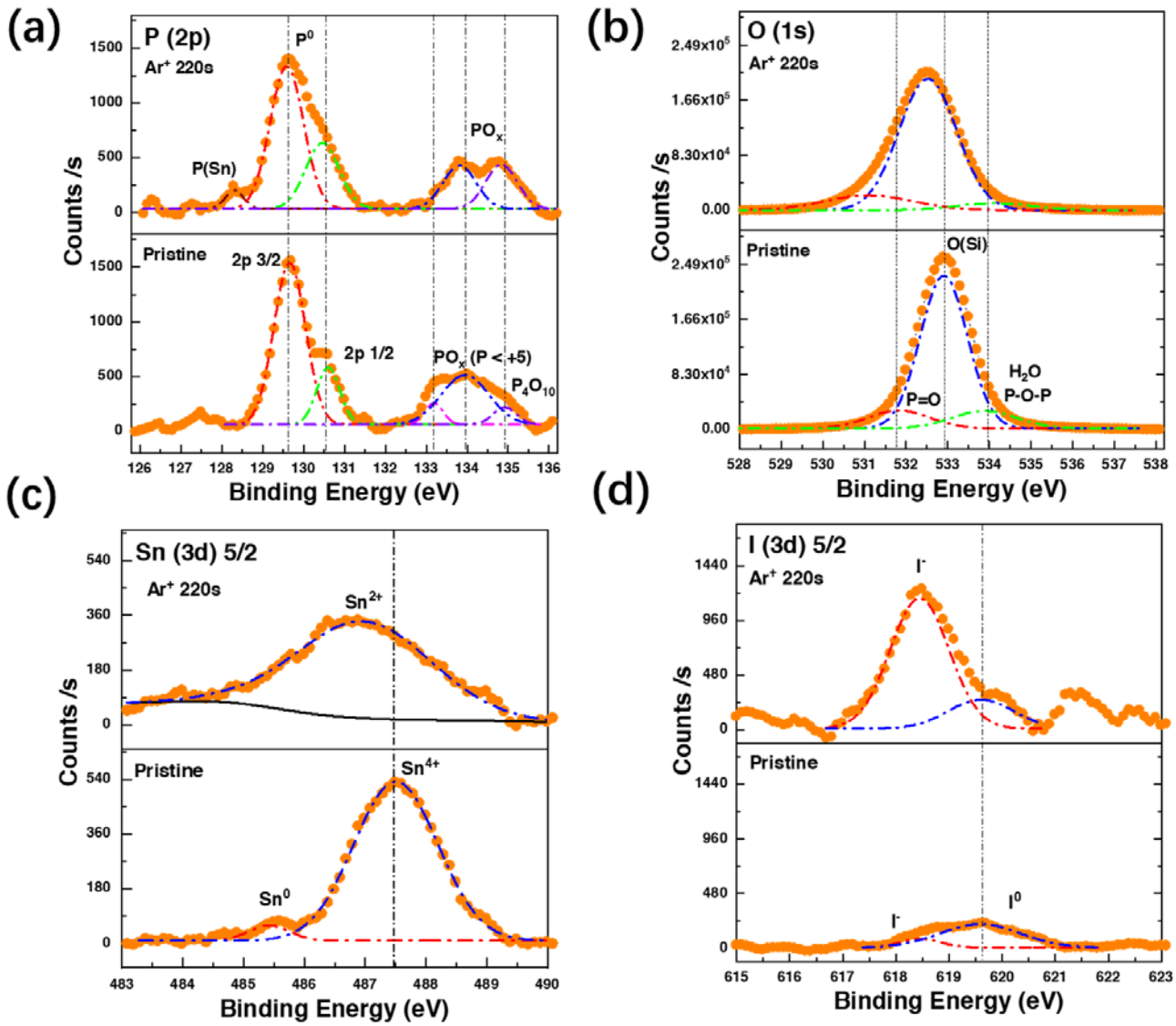

Figure 4. High-resolution XPS of VP crystals before and after Ar^+ plasma treatment. (a-d) XPS spectra of the elemental P (*2p*), O (*1s*), Sn (*3d*) and I (*3d*) cores of the VP crystal before (lower panels) and after (upper panels) 220 s Ar^+ plasma treatment.

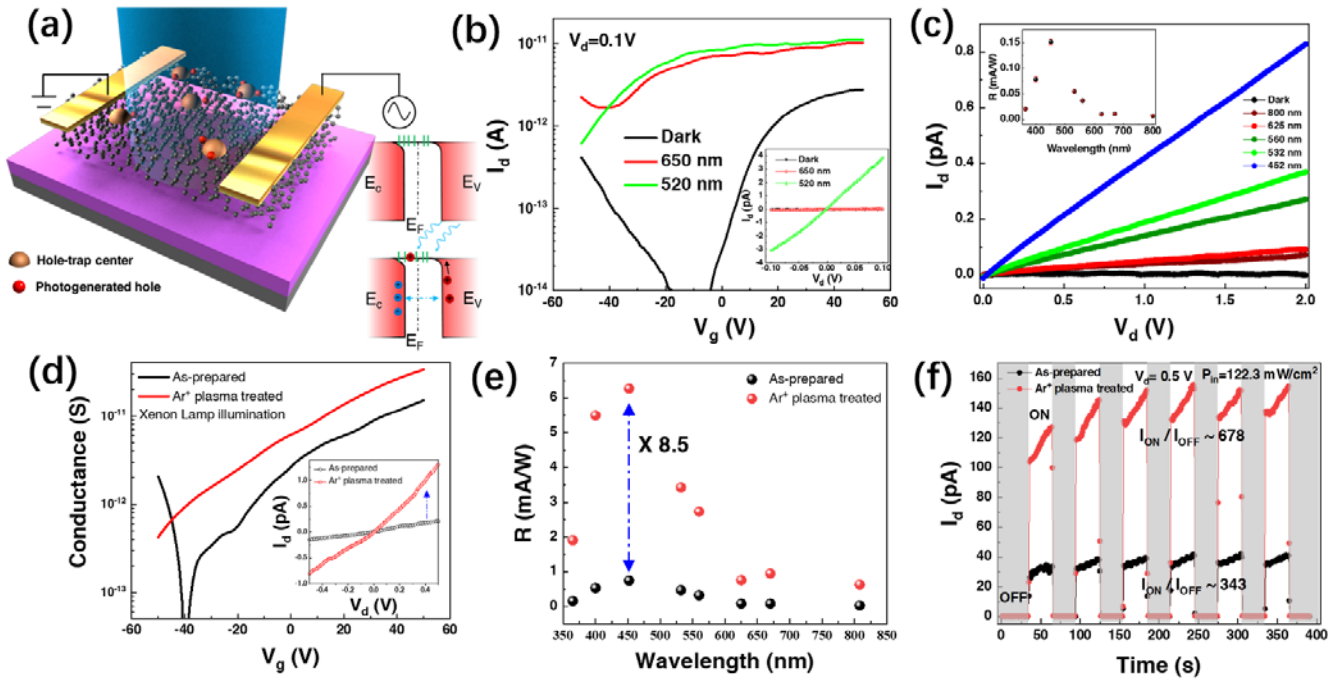

Figure 5. Ar^+ plasma induced changes of the optoelectronic properties in VP phototransistors. (a) Schematic illustration of the VP phototransistor measurement under illumination based on the hole-trapping mechanism. The yellow hemispheres (red balls) represent hole-trap centres (photogenerated holes). The insets are the corresponding band diagrams of the top surface regions of the VP channel in dark (upper one) and under illumination (lower one), respectively. (b) Transfer characteristics of the VP phototransistor in the dark, 650 nm and 520 nm laser diode illumination with the power density of $P_{in} \approx 29.2$ mW/cm^2. The inset gives the corresponding I-V curves. (c) I-V curves of the VP phototransistor under illumination with different wavelengths. The illumination light source was a 300 W xenon lamp filtered by ultra-narrow bandpass filters with different central wavelengths. Inset shows the wavelength-dependent responsivity of the VP phototransistor. (d) Comparison of the transfer curves of as-prepared (black) and 120 s Ar^+ plasma treated (red) VP phototransistor. The light source is the xenon lamp without filters. The inset illustrates the corresponding I-V curves. (e)

Comparison of the calculated responsivities of the as-prepared (black) and plasma treated (red) VP phototransistor under illumination with various wavelengths. (f) Time-dependent photoresponse excited by a 445 nm pulsed laser for the as-prepared (black) and plasma treated (red) VP phototransistor. The photocurrent switching on/off ratio exhibits significant increase in the treated one. The applied V_d was 0.5 V and the incident laser power density P_{in} was 122.3 mW/cm^2.

Table of Contents

A novel layered material, violet phosphorus (VP), possesses robust trionic effect with a huge trion binding energy of ~ 109 meV. With the trion-exciton conversion by Ar^+ plasma exposure, VP's photoluminescence can be modulated based on a combined effect, which is related to the reduction of the population of stannus Sn-I-P imputrities and electron withdrawal by the surface defects.

Yanyong Li, Songhua Cai, Wai Kin Lai, Chenhao Wang, Lukas Rogée, Lyuchao Zhuang, Lingling Zhai, Shenghuang Lin, Mingjie Li and Shu Ping Lau*

Impurity-Induced Robust Trionic Effect in Layered Violet Phosphorus